A Bulk-Micromachined Three-Axis Capacitive MEMS Accelerometer on a Single Die

Serdar Tez, Ulas Aykutlu, Mustafa Mert Torunbalci, and Tayfun Akin

***Abstract*— This paper presents a high-performance three-axis capacitive microelectromechanical system (MEMS) accelerometer implemented by fabricating individual lateral and vertical differential accelerometers in the same die. The fabrication process is based on the formation of a glass-silicon-glass multi-stack. First, a 35-μm thick ⟨111⟩ silicon structural layer of an Silicon-On-Insulator (SOI) wafer is patterned with deep reactive ion etching (DRIE) and attached on a base glass substrate with anodic bonding, whose handle layer is later removed. Next, the second glass wafer is placed on the top of the structure not only for allowing to implement a top electrode for the vertical accelerometer, but also for acting as an inherent cap for the entire structure. The fabricated three-axis MEMS capacitive accelerometer die measures $12 \times 7 \times 1$ mm^3. The x-axis and y-axis accelerometers demonstrate measured noise floors and bias instabilities equal to or better than 5.5 μg/$\sqrt{\text{Hz}}$ and 2.2 μg, respectively, while the z-axis accelerometer demonstrates 12.6 μg/$\sqrt{\text{Hz}}$ noise floor and 17.4 μg bias instability values using hybrid-connected fourth-order sigma–delta CMOS application specific integrated circuit (ASIC) chips. These low noise performances are achieved with a measurement range of over $\pm$10 g for the x-axis and y-axis accelerometers and +12/−7.5 g for the z-axis accelerometer, suggesting their potential use in navigation grade applications. [2014-0351]**

***Index Terms*— Three-axis capacitive microelectromechanical system (MEMS) accelerometer, glass-silicon-glass, double glass modified silicon on glass (DGM-SOG).**

I. Introduction

MICROELECTROMECHANICAL systems (MEMS) using the capacitive transduction have been attracted attention especially in the last decades, as a result of unique features, such as low-cost, small-size, and high-reliability. Today micromachined capacitive sensors are used in many different applications with many different requirements. One of the most widely used capacitive sensors is the accelerometer, finding applications in high volume products that do not require high performance, such as smart phones, tablets, gaming systems, TV remote control systems, and toys, as well as low volume products requiring high performance, i.e., low noise floor, low cross-axis sensitivity, and high dynamic range [1]. Most of these applications require three-axis acceleration sensing, and therefore, there is an intensive study in the literature to implement high performance three-axis MEMS accelerometers, where different design concepts and various fabrication approaches are taken into consideration.

The most straight forward approach for implementing three-axis MEMS accelerometers is to assemble three individual and identical accelerometers orthogonally on a discrete package [2]. For this approach, the fabrication method of the accelerometer is not critical: it can be a lateral accelerometer fabricated using post-CMOS [3], surface [4], and bulk micromachining [5], [6], or it can be a vertical differential accelerometer implemented using multi-stack structures with multiple bonding processes necessary for achieving both the bottom and top electrodes [7]–[9]. Some of these approaches can only provide limited performances due to their small structural thicknesses, in addition to other limitations like buckling due to high internal stress. Some of them can provide very high performances for acceleration measurement from single axis, however, implementing three-axis MEMS accelerometers by assembling three individual and identical accelerometers orthogonally on a discrete package require complex packaging procedures and end up occupying large volumes in the final packaged device. Furthermore, they suffer from mistakes in orthogonal alignments. These problems can be solved with a different extreme approach, i.e., by using a single proof mass but multiple electrodes for sensing three different axes [10]–[12]. This approach results in extremely small size devices, but suffer from cross-axis sensitivity, limiting their use in high performance applications. An extension of this approach is the concentric approach, i.e., placing multiple proof masses for each axis orthogonally on the same substrate [13]. However, these type accelerometers have non-identical sensing elements, i.e., different mass shapes and spring structures for each axis, resulting in undesirably different performance characteristics, especially for high performance applications.

Most of the problems of all of these accelerometers can be overcome by implementing three individual accelerometers

Manuscript received November 18, 2014; revised June 17, 2015; accepted June 23, 2015. Date of publication August 6, 2015; date of current version September 29, 2015. This work was supported by the State Planning Organization (DPT) of Turkey (currently the Ministry of Development) within the Industrial Micro-Electro-Mechanical Systems Project. Subject Editor P. M. Sarro.

S. Tez was with the Micro and Nanotechnology Program, Middle East Technical University, Ankara 06800, Turkey, and also with the Micro-Electro-Mechanical Systems Research and Applications Center, Middle East Technical University, Ankara 06800, Turkey. He is now with the Department of Electrical and Electronics Engineering, Pamukkale University, Denizli 20070, Turkey (e-mail: stez@pau.edu.tr).

U. Aykutlu and T. Akin are with the Department of Electrical and Electronics Engineering, Middle East Technical University, Ankara 06800, Turkey. They are also with the Micro-Electro-Mechanical Systems Research and Applications Center, Ankara 06800, Turkey (e-mail: uaykutlu@mems.metu.edu.tr; tayfun-akin@metu.edu.tr).

M. M. Torunbalci was with the Micro and Nanotechnology Program, Middle East Technical University, Ankara 06800, Turkey. He is now with the Micro-Electro-Mechanical Systems Research and Applications Center, Ankara 06800, Turkey (e-mail: mtorunbalci@mems.metu.edu.tr).

Color versions of one or more of the figures in this paper are available online at http://ieeexplore.ieee.org.

Digital Object Identifier 10.1109/JMEMS.2015.2451079

1057-7157 © 2015 IEEE. Personal use is permitted, but republication/redistribution requires IEEE permission.
See http://www.ieee.org/publications_standards/publications/rights/index.html for more information.

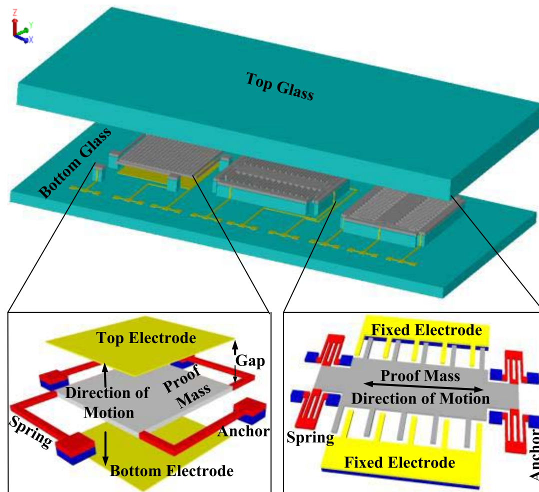

Fig. 1. The design concept of the three-axis accelerometer.

on a single die, where the orthogonal alignment of the accelerometers can inherently be achieved in the fabrication process. There are already commercially available [14], [15] and academically reported [16], [17] three-axis accelerometers implemented with this approach by using different fabrication methods. However, most of these three-axis accelerometers have either high noise values [14], [15], [17] or very limited measurement range [16], restricting their use in high performance applications. Therefore, there is a need to develop a new fabrication approach for implementing three individual high performance accelerometers on a single die, i.e., resulting in a small area compared to assembling three individual accelerometers orthogonally on a discrete package, where each accelerometer provides low noise and high measurement range with low cross-axis sensitivity.

This paper reports the development of such a high performance three-axis capacitive MEMS accelerometer with low cross-axis sensitivity, where the orthogonal alignment of the accelerometers can inherently be achieved in a special fabrication process that is developed to result in low noise and high measurement range for all of the measurement axis. The fabrication process is based on the Double Glass Modified Silicon-on-Glass (DGM-SOG) fabrication process [18], where a glass-silicon-glass multi-stack structure is possible to implement, allowing to form individual lateral and vertical accelerometers on the same die. The top glass layer is used not only for implementing a top electrode for the vertical accelerometer but also for forming an inherent cap for the entire structure. This fabrication approach allows selecting various structural thicknesses, wafer orientation as well as doping concentration of the silicon wafer considering the performance parameters of the desired accelerometer. The system level performance parameters of the individual accelerometers are measured by connecting them to fourth order sigma-delta CMOS ASIC chips.

II. Design

Figure 1 shows the conceptual design of the three-axis accelerometer, illustrating the implementation of the lateral and vertical differential accelerometers on a same die by using a glass-silicon-glass multi-stack structure. The two lateral differential accelerometers are easily implemented by attaching a single crystal silicon structural layer to a glass wafer. The same structure can be used to implement single sided vertical accelerometer, but this limits its performance. For a high performance vertical accelerometer, a differential structure is preferred, which is achieved here by attaching a second glass wafer; this second glass wafer also acts as an inherent cap for the entire structure.

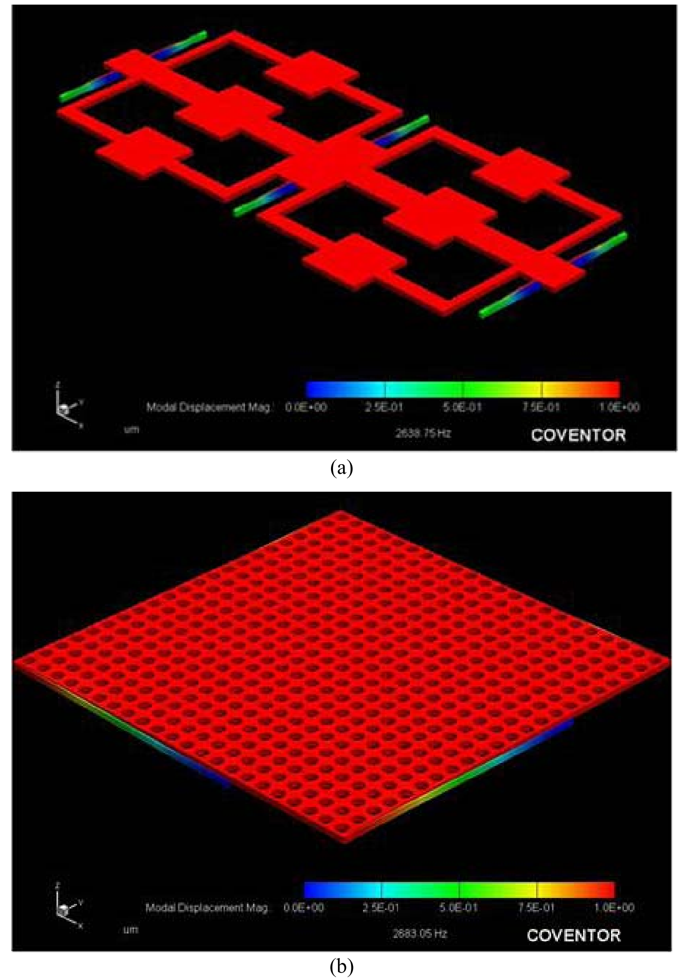

Fig. 2. FEM simulation. The resonance frequencies are (a) 2638 Hz for the lateral accelerometer (b) 2683 Hz for the vertical accelerometer.

The lateral accelerometer is composed of three main mechanical structures: springs, the proof mass and capacitive fingers. The movable part of the accelerometer is the proof mass region, and it is attached to the anchor region with the help of the spring structures. The springs are placed to both ends and to the middle of the accelerometer to prevent undesired movement of the accelerometer as much as possible. There are capacitive fingers on both sides of the accelerometer. Furthermore, capacitive fingers are placed at both sides and center of the lateral accelerometer for increasing the sensitivity and for decreasing the proof mass amount. In the rest position of the proof mass, the capacitances of both sides are equal to each other. The design of the lateral accelerometer allows the

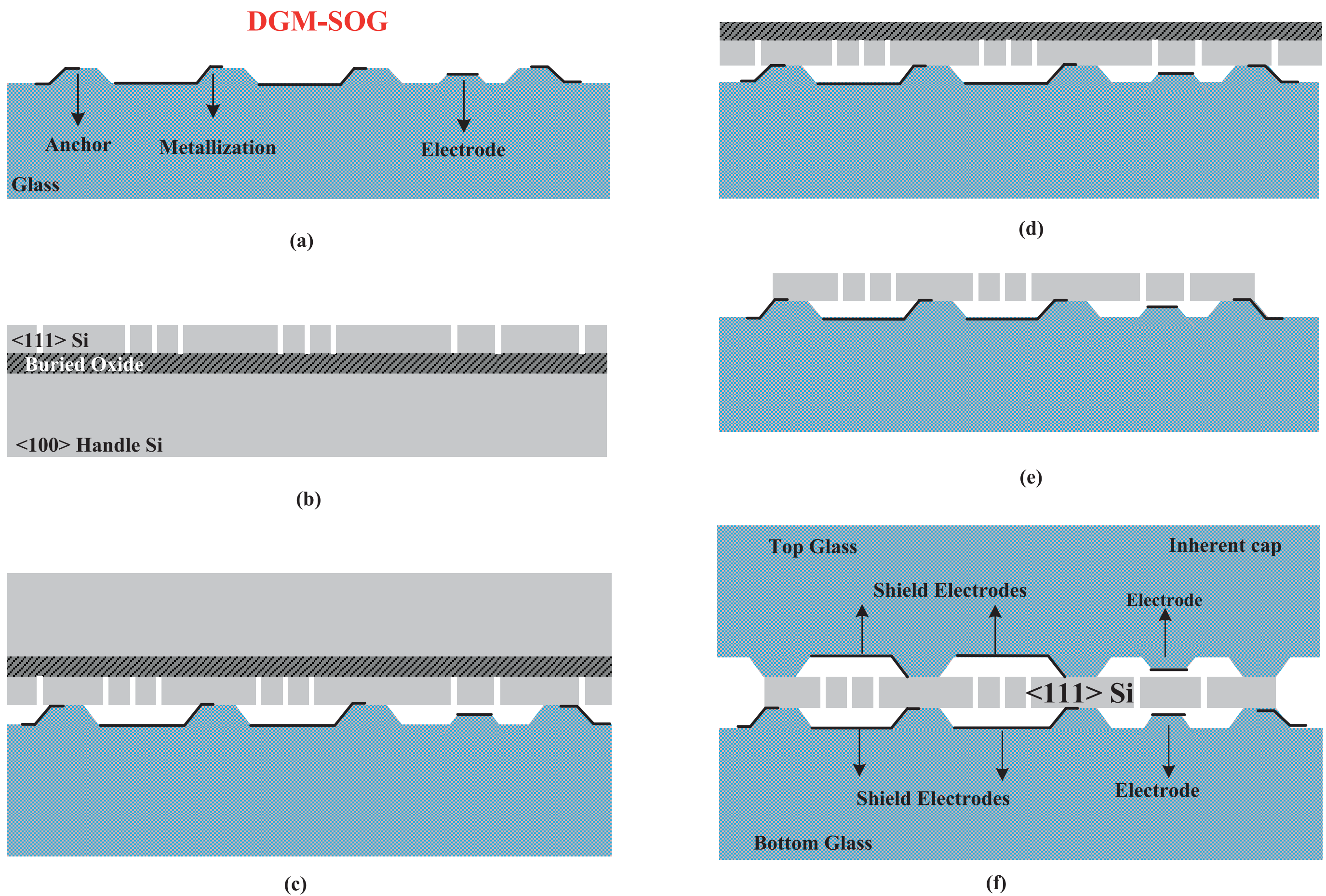

Fig. 3. The fabrication process step of the three-axis accelerometer. (a) Formation of anchors and metal lines on glass substrate. (b) Patterning of device layer until buried oxide etch-stop. (c) The anodic bonding step. (d) Removal of handle layer by DRIE. (e) Removal of the buried oxide layer by BHF and release process. (f) The second anodic bonding step

motion of the proof mass at in-plane directions. In the presence of the acceleration, the proof mass deflects to the opposite side of the acceleration, changing the capacitance formed between the fingers of the proof mass and fixed electrodes on both sides. Thus, the acceleration can be determined with a readout circuit having closed-loop architecture by differentially reading the capacitance changes.

The vertical accelerometer has a crab-leg structure to provide motion of the vertical accelerometer in the z-axis direction. The capacitance is formed by implementing electrodes placed on the top and bottom side of the proof mass, where the capacitive gap is selected as 2 μm.

The proof mass of the vertical accelerometer has perforation holes for decreasing not only the damping coefficient but also the proof mass amount. In the existence of the acceleration, the proof mass deflects to the opposite side of the acceleration, changing the capacitance formed between the bottom electrode and the proof mass as well as the top electrode and the proof mass. Thus, a closed-loop readout circuit can be utilized to determine the acceleration by differentially, reading the capacitance changes of both sides. During the design of the three-axis accelerometer, it is difficult to obtain same performance parameters for both the lateral and the vertical accelerometers.

Figure 2 shows the Finite Element Method (FEM) simulation results of the lateral and the vertical accelerometers. The mass of the fingers are uniformly distributed to the mass of the proof mass of the lateral accelerometer during the simulation for simplicity. Table I shows design parameters of lateral and vertical accelerometers. Table II gives the comparison of the simulation results with hand calculation.

III. Fabrication

Figure 3 shows the fabrication process steps for the three-axis capacitive MEMS accelerometer. The fabrication process is based on the DGM-SOG fabrication process reported in [18] with reduced mask steps.

The fabrication process starts with the capacitive gap formation for the vertical accelerometer on the bottom and the top glass wafers, followed by the anchor regions formation and pad metallization, as shown in Figure 3 (a). In this step, recesses are formed among the anchors to transfer the pad metal to external world, i.e., sensors are not hermetically sealed in the die level. The pad metallization mask also includes the shield metallization to prevent the bonding of the suspended structure to the top glass during the second anodic

TABLE I
DESIGN PARAMETERS OF THE LATERAL AND VERTICAL ACCELEROMETERS

Design Parameters	Lateral	Vertical
Structural Thickness (µm)	35	35
Proof Mass (kg)	2.06 x 10^{-7}	2.43 x 10^{-7}
Spring Constant (N/m)	50.8	49.7
Resonance Frequency (Hz)	2495	2278
Capacitive Gap (µm)	2	2
Capacitive Anti-Gap (µm)	7	-
Finger Length (µm)	155	-
Electrode Area $(µm)^2$	-	2200 x 2200
Brownian Noise (µg/√Hz)	5.73	5.56
Rest Capacitance (pF)	10.4	13.2

TABLE II
SIMULATION RESULTS VERSUS HAND CALCULATION

Lateral Accelerometer	Hand Calculations	Simulation Results
Proof Mass (kg)	2.06 x 10^{-7}	2.05 x 10^{-7}
Resonance Frequency (Hz)	2495	2638
Vertical Accelerometer	**Hand Calculations**	**Simulation Results**
Proof Mass (kg)	2.43 x 10^{-7}	2.46 x 10^{-7}
Resonance Frequency (Hz)	2278	2683

bonding, as multi-stack is formed by using the two-step anodic bonding. The silicon wafer part of the multi-stack is processed using an SOI wafer, where the structures are patterned by using DRIE (Figure 3 (b)). The next step is to anodically bond the bottom glass and the silicon wafer (Figure 3 (c)). Afterwards, the handle layer of the SOI wafer is completely removed until the buried oxide layer (BOX) by using DRIE (Figure 3 (d)). Finally, the BOX layer is etched by using BHF to suspend structures (Figure 3 (e)).

After this step, the buckling amount of the proof mass of the vertical accelerometer is observed by using the optical profiler. Figure 4 shows the buckling measurement results of the proof mass of the vertical accelerometer before the last anodic bonding step, where a 0.2 μm buckling is observed in the direction of x- and y- axis of the proof mass of the vertical accelerometer. The main reason of this is most probably related with mismatch in the coefficient of thermal expansion (CTE) of the glass and silicon wafers corresponding to the anodic bonding temperature and room temperature. This leads to the capacitance mismatch, resulting in nonsymmetrical acceleration measurement range in the z-axis.

The final and the most critical step in the three-axis accelerometer fabrication is to form the glass-silicon-glass multi-stack by using the second anodic bonding (Figure 3 (f)). The glass-silicon-glass anodic bonding is believed to be a complicated process since the bottom glass electrically isolates the silicon layer from the bonding potential. Different solutions have been proposed for the multi-stack anodic bonding where special bonding equipment [19] or complicated electrical models are used [20]. In this work, the top glass is anodically bonded to previously formed silicon-glass stack where flags with 25 μm-thick are used to provide the bonding potential to the sandwiched silicon layer without requiring any special bonding equipment or using any complicated electrical model. Figure 5 presents the scheme of the anodic bonding of glass-silicon-glass multi-stack. Figure 6 shows the fabricated sensor wafer.

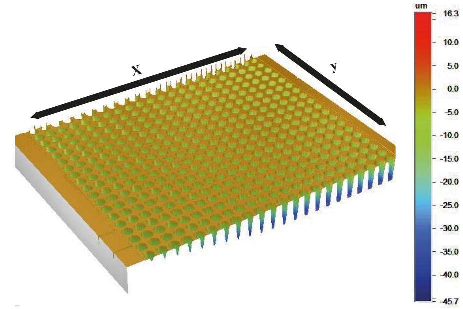

(a)

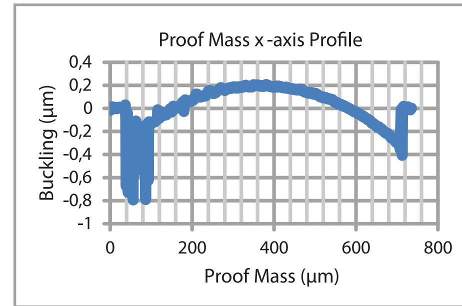

(b)

Fig. 4. (a) The buckling for the proof mass of the vertical accelerometer is measured by using the optical profiler (b) The observed buckling in z-axis direction is nearly 0.2 μm in the direction of x- and y- axis of the proof mass of the vertical accelerometer.

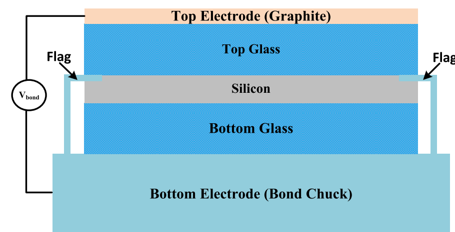

Fig. 5. The scheme of the anodic bonding of the glass-silicon-glass multi-stack.

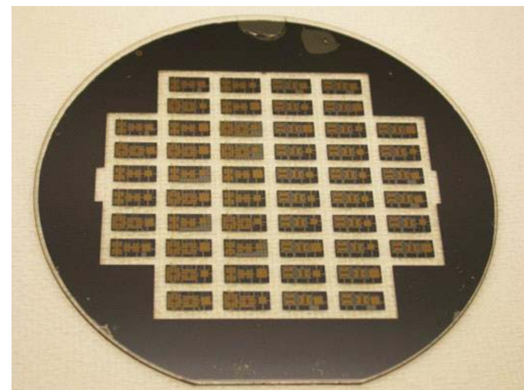

Fig. 6. The fabricated three-axis accelerometer wafer.

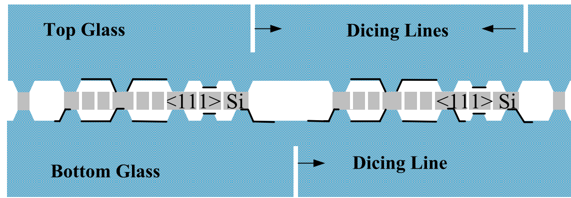

Fig. 7. The representation of the two-step dicing process.

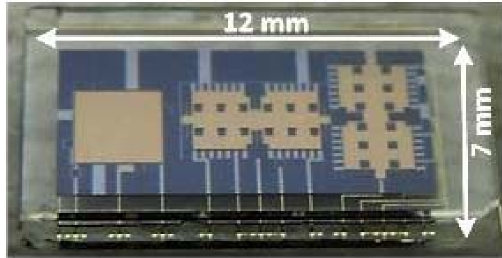

Fig. 8. The fabricated three-axis accelerometer.

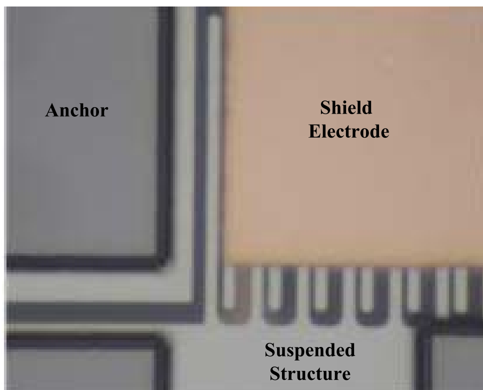

Fig. 9. The photograph of the suspended structure after the second anodic bonding, where the shield metallization prevents the stiction of the suspended structure to the top glass layer.

The next step is to dice the fabricated wafer and uncover the pad metallization for wire bonding. The dicing of the multi-stack structure is challenging problem due to the risk of leaking water inside to the sensor region during the dicing process, especially if each die is not hermetically sealed, which is the case here. Figure 7 shows the applied dicing process for the multi-stack type three-axis accelerometer. Firstly, the top glass side of the fabricated wafer is partially cut, and the same dicing step is applied to the bottom glass side of the fabricated wafer. Then, sensors are manually separated from each other. It should be noted here that the hermetically sealing of the glass-silicon-glass multi-stack structure is ensured in the wafer level during the multiple anodic bonding processes covering the edge regions. It should also be noted that the dicing line of the bottom side and the top side of the wafer is intentionally determined from different region to uncover the pad metallization.

Figure 8 shows the diced three-axis accelerometer die, which measures 12 mm × 7 mm × 1 mm. Figure 9 shows the photograph of the suspended structure after the second anodic bonding, where the shield metallization prevents the stiction of the suspended structure to the top glass layer. Figure 10 shows an SEM image of the fabricated three-axis capacitive MEMS accelerometer. This image clearly shows the details of shield electrode, suspended silicon structure, and interface of the glass-silicon-glass multi-stack.

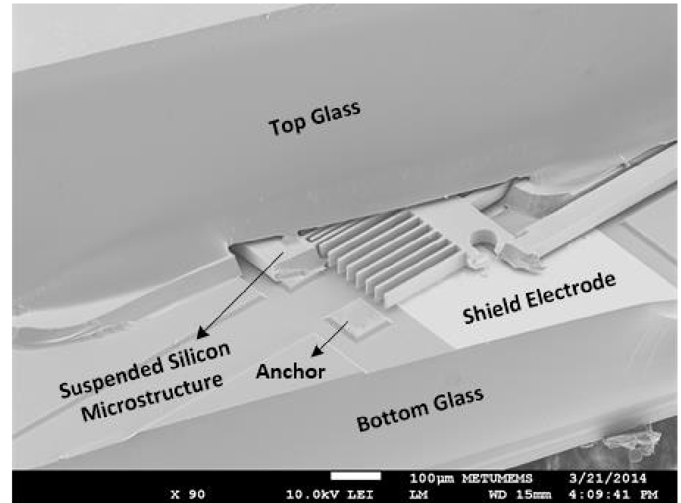

Fig. 10. An SEM image of the fabricated device showing the glass-silicon-glass interface.

TABLE III
THE SENSOR CONNECTION DIAGRAM WITH RESPECT TO PATH NUMBERS

Pad #	Lateral	Vertical
1	Fixed electrode	Top Electrode
2	Fixed electrode	Bottom Electrode
3	Proof mass	Proof mass
4	Bottom shield electrode	-
5	Top shield electrode	-

IV. SENSOR LEVEL TEST RESULTS

A. Capacitance-Voltage (C-V) Change

The functionality of the three-axis accelerometer implemented with the lateral and vertical accelerometers on the same die is separately determined by the capacitance-voltage change test, where a DC bias is applied to the proof mass and one of the electrodes, while the other electrode is connected to ground. For the lateral accelerometers, there are shield electrodes placed at both the bottom and top glass layers, occupying an area corresponding to the entire suspended structure. These shield electrodes are temporally shorted to the proof mass during the fabrication to prevent the bonding of the proof mass to the top or bottom glass layers. After the fabrication, they are separated from the proof mass by using the laser cutting system. These shield electrodes should be connected to the ground layer during the sensor operation to prevent any parasitic capacitance that they present. The connection of the shield electrodes to ground should also be realized during C-V measurements to obtain measurement results consistent with the designed values.

Table III summarizes a diagram explaining the pad number with respect to the sensor connection, where the pad number 1-2 represents both the fixed electrodes connections for lateral and vertical accelerometers. The pad number 3 indicates the

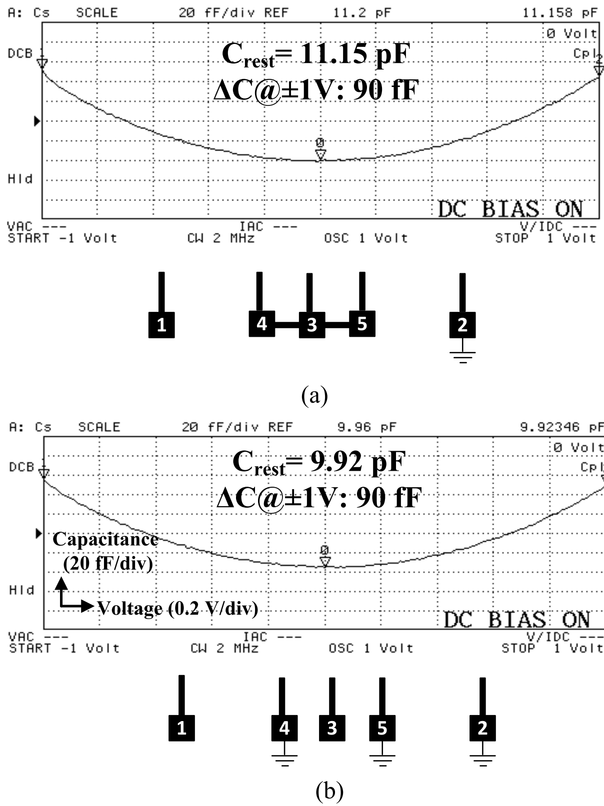

Fig. 11. The C-V measurement result of the lateral accelerometer. (a) The capacitance formed between pad number 1 and pad number 3 is measured while pad number 2 is grounded. (b) The capacitance formed between pad number 1 and pad number 3 is measured while pad number 2, pad number 4 and pad number 5 are grounded.

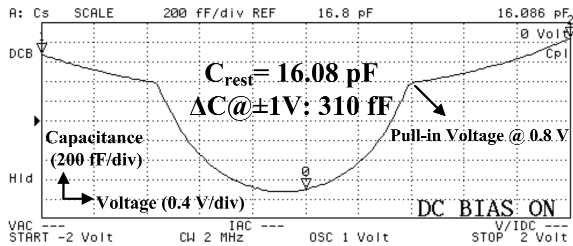

Fig. 12. C-V measurement result of the vertical accelerometer.

proof mass connection, while the pad number 4-5 denotes the bottom and top shield electrode connections.

Figure 11 shows the C-V measurement results with respect to the pad metallization configuration for the lateral accelerometers. The test results and the theoretical calculations are in good agreement with each other. However, it should be noted that the fabrication process introduces parasitic capacitances to lateral accelerometers. Figure 12 shows the measurement result for the capacitance formed between the bottom electrode and the proof mass of the vertical accelerometer. Table IV shows the comparison of theoretical and measured values for the rest capacitance of the lateral and vertical accelerometers. The measured capacitances of lateral accelerometers are very close to the designed values and close to each other. The slight reduction could be coming from the undercut during the DRIE step. The measured capacitances of the vertical accelerometers are higher than

TABLE IV

THE C-V MEASUREMENT RESULTS

Rest Capacitance (pF)	Designed		Measurement	
	C_1	C_2	C_1	C_2
Lateral	10.4	10.4	9.92	9.73
Vertical	13.2	13.2	16.08	13.95

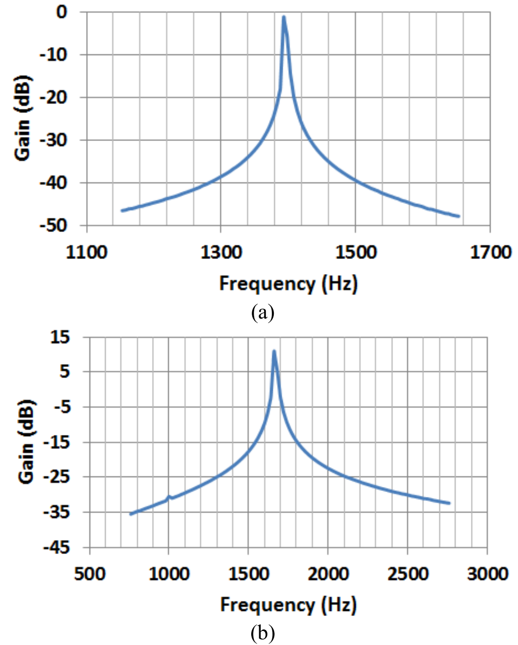

Fig. 13. The resonance frequency measurement results for (a) lateral and (b) vertical accelerometers.

TABLE V

SIMULATION VERSUS MEASUREMENT RESULTS OF THE RESONANCE FREQUENCY OF THE THREE-AXIS ACCELEROMETER

Lateral Accelerometer	Sim. Results	Meas. Results
Resonance Frequency (Hz)	2638	1400
Vertical Accelerometer	**Sim. Results**	**Meas. Results**
Resonance Frequency (Hz)	2683	1660

the designed value, probably due to the fringing field effects that were not considered in the design. The difference in the differential capacitances is due to the buckling of the structural layer due to stress.

B. Resonance Frequency Measurements

The resonance frequencies of accelerometers are individually measured to determine the functionality of the lateral and vertical accelerometers using a dynamic signal analyzer. The accelerometers are actuated with an AC signal at frequencies ranging from 1 kHz to 3 kHz while the proof mass is biased with a DC voltage of 2 V under a controlled vacuum environment. Figure 13 shows the resonance characteristics of the lateral and vertical accelerometers. Table V summarizes simulation versus measurement results of the resonance frequencies of the three-axis accelerometer. It should be noted that there is a significant mismatch between the simulation

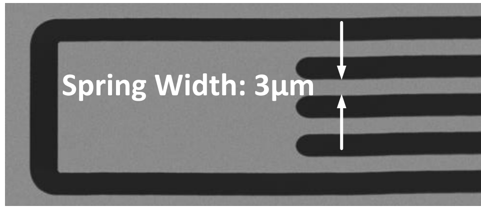

Fig. 14. The SEM image of the spring structure after DRIE etch. The SEM observation shows that the spring width is 75% of its design value after the DRIE etch.

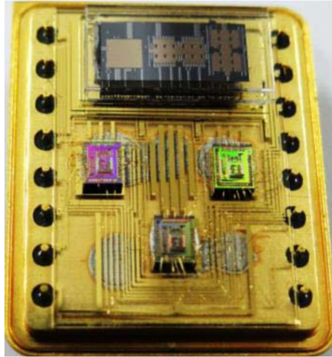

Fig. 15. The three-axis accelerometer package. The three-axis accelerometer is connected to three individual readout circuit reported in [21] by a hybrid glass substrate.

and measurement results, which is mainly related with the variations in device dimensions compared to the design values, as a result of the mask fabrication, lithography steps, as well as the thinning of spring structures during the DRIE etch in the fabrication. Figure 14 shows the spring structures whose width reduces to 75% of its design value after the DRIE etch.

V. The System Level Test Results

The tested three-axis accelerometer is integrated with the CMOS readout circuit reported in [21] to prepare a hybrid three-axis accelerometer package at the atmospheric pressure. Figure 15 shows the prepared hybrid three-axis accelerometer package. During the system level tests, the one bit output data have been collected at a 500 kHz sampling frequency and decimated to obtain approximately 250 Hz sampling rate. Figure 16 shows the Power Spectral Density (PSD) of one bit output for x-, y-, and z- axis accelerometers. The noise floors of the lateral and the vertical accelerometers are about -105 dBg/$\sqrt{\text{Hz}}$ and -98 dBg/$\sqrt{\text{Hz}}$, respectively.

Figure 17 shows the Allan Variance test results of lateral and vertical accelerometers. The noise floors of lateral and vertical accelerometers are extracted from both the Allan Variance and PSD graphs. The bias instability values are also extracted from the Allan Variance plots fitting to a slope of 0. The bias instability values of the lateral and vertical accelerometers are 2.2 μg, 1.7 μg, and 17.4 μg, respectively. Non-linearity of the three-axis accelerometer is measured by using the centrifuge. The non-linearity data are evaluated with respect to the best fit, and non-linearity measurement results of the three-axis accelerometer are 0.34 %, 0.28 %, and 0.41 % for x-, y-, and z-axis, respectively. Figure 18 shows the non-linearity result of the three-axis accelerometer.

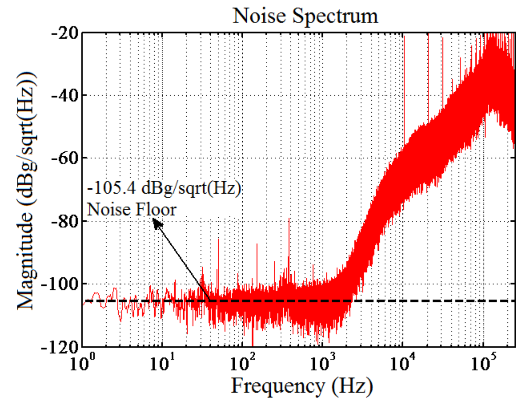

(a)

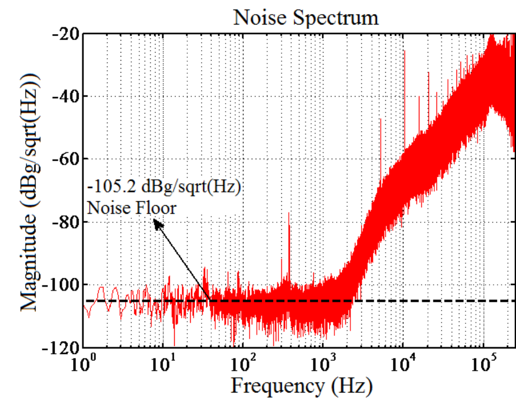

(b)

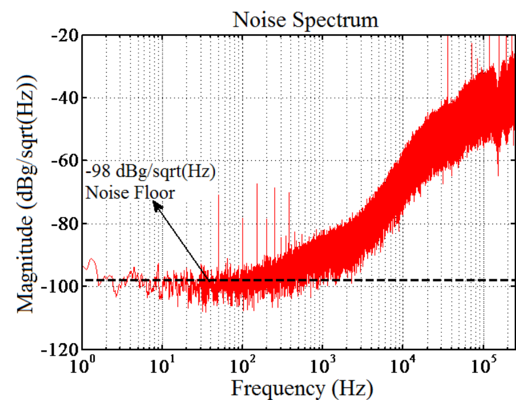

(c)

Fig. 16. Power Spectral Density (PSD) (a) -105.4 dBg/$\sqrt{\text{Hz}}$ noise floor for x-axis and (b) -105.2 dBg/$\sqrt{\text{Hz}}$ noise floor for y-axis (c) -98 dBg/$\sqrt{\text{Hz}}$ noise floor for z-axis accelerometers.

TABLE VI
Cross-Axis Sensitivity Results of the Three-Axis Accelerometer

Acceleration Input	Output x	Output y	Output z
x	-	0.99%	0.81%
y	0.56%	-	0.62%
z	0.21%	0.56%	-

The cross-axis sensitivity of the fabricated three-axis accelerometer is also determined by applying $\pm$1g with rotating the test system around one axis while the acceleration

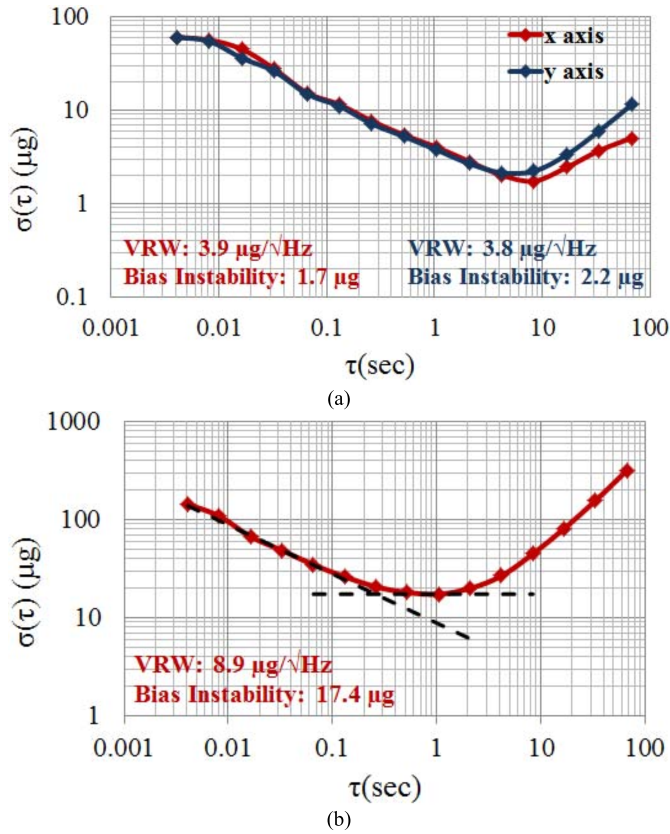

Fig. 17. Allan Variance results showing the velocity random walk (VRW) and the bias instabilities for (a) x- and y- (b) z-axis accelerometers.

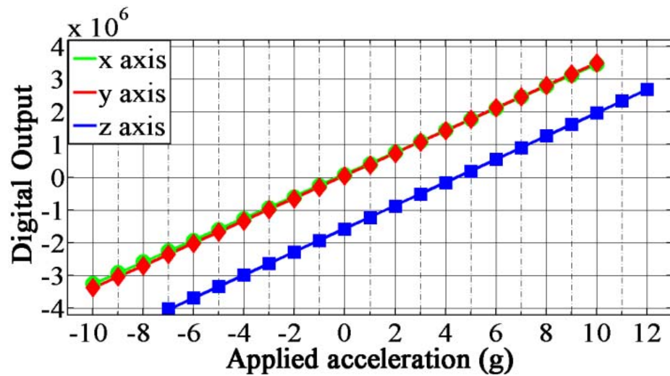

Fig. 18. Linearity test results of the three-axis accelerometer, which shows 0.34 %, 0.28 %, and 0.41 % non-linearity for x-, y-, and z- axis, respectively. Note that x- and y- axis results overlap.

TABLE VII
THE PERFORMANCE RESULTS OF THE THREE-AXIS ACCELEROMETER

	x	y	z
Noise (μg/√Hz)	5.4	5.5	12.6
Bias Instability(μg)	2.2	1.7	17.4
Measured Range (g)	±10	±10	+12/-7.5
Expected Range	+12.1/-12.8	+12.0/-12.4	+16.2/-7.5
Non-linearity	0.34%	0.28%	0.41%

data have simultaneously been collected for all three axes. Then, the cross-axis sensitivity of the three-axis accelerometer is extracted from the collected data. Table VI shows the cross-axis sensitivity results of the three-axis accelerometer.

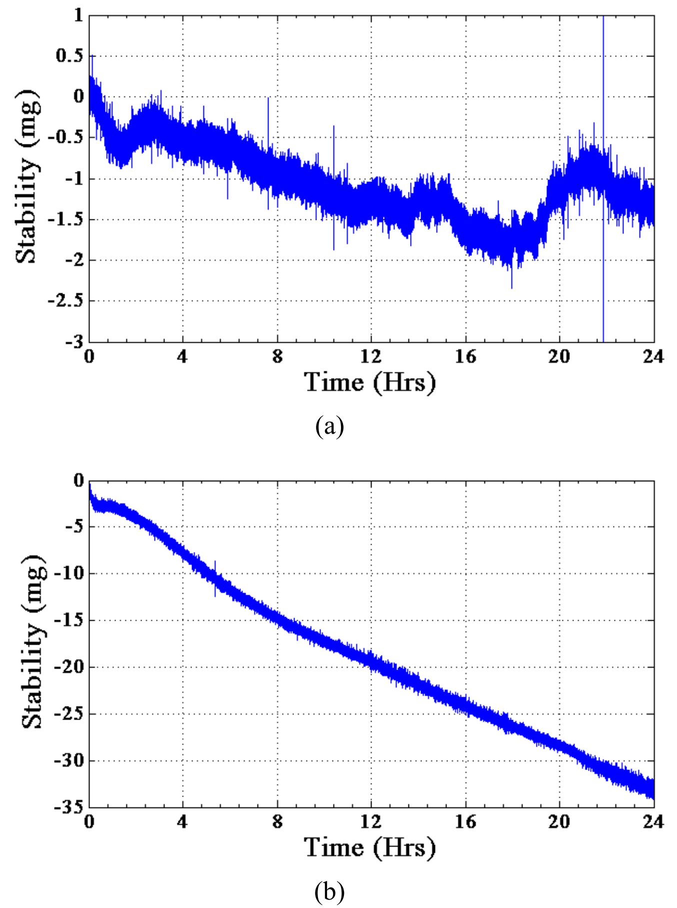

Fig. 19. The long term stability measurement data of (a) the lateral and (b) vertical accelerometers. The lateral and the vertical accelerometers have 2 mg and 35 mg output drift over 24 hours, respectively.

It should be noted that the placement of the sensor on the hybrid package is still a source of misalignment, which leads to cross-axis sensitivity although the fabrication process ensures the orthogonal alignment.

Table VII summarizes the system level performance result for the fabricated three-axis accelerometer. The x- and y-axis accelerometers demonstrate measured noise floors and bias instabilities equal to or better than 5.5 μg/$\sqrt{\text{Hz}}$ and 2.2 μg, respectively, while the z-axis accelerometer demonstrates 12.6 μg/$\sqrt{\text{Hz}}$ noise floor and 17.4 μg bias instability values using hybrid-connected fourth-order sigma-delta CMOS ASIC chips reported in [21]. These low noise performances are achieved with a measurement range of over $\pm$10 g for the x- and y-axis accelerometers and $+12/-7.5$ g for the z-axis accelerometer.

The long term stabilities of the lateral and vertical accelerometers are also observed. The long term stability test is performed in the room temperature over 24 hours. The long term bias stability measurements of the lateral and vertical accelerometers have demonstrated 2 mg and 35 mg output drift over 24 hours, respectively. Figure 19 shows the long term stability measurement data for the lateral and vertical accelerometers.

The temperature sensitivity test is also conducted for the three-axis accelerometer. The temperature characterization is

TABLE VIII
THE COMPARISON OF PERFORMANCE RESULTS OF THE THREE-AXIS ACCELEROMETERS IMPLEMENTED ON THE SAME DIE

References	Noise (μg/√Hz)			Range (g)	Cross-Axis	Non-linearity
	x	y	z			
[12]	120000	271000	357000	Meas. Range ±0.8~6	< 8.33%	2.64%, 3.15% and 3.36%
[14]	2700	2700	4300	±200	±1.4%	±0.5%
[15]	280	280	350	±3.6	±1%	±0.3%
[16]	1.6	1.6	1.08	±1	-	-
[17]	400	200	900	Meas. Range 0.01~2	3%, 2.3 % and 8.8%	1%, 0.5% and 2.4%
[22]	2100	2000	2100	Meas. Range 0.01~1	< 6.6%	3.2% , 1.4%, and 2.8%
[23]	12	14	110	3.2 for lateral, 5.1 for vertical	< 4.73%	-
[24]	150			±2, ±4, ±8, ±16	-	-
[25]	15000			±100	-	2%
[26]	99			±2, ±4, ±8	-	-
[27]	218			±2, ±4, ±8	±5%	-
This Study	5.4	5.5	12.6	±10 for lateral +12/-7.5 for vertical	< 1%	0.34 % , 0.28 %, and 0.41 %

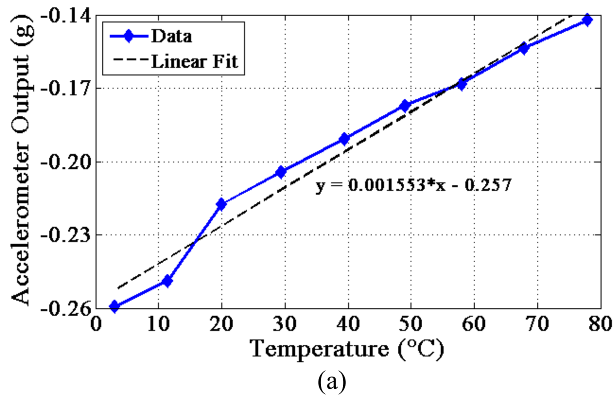

(a)

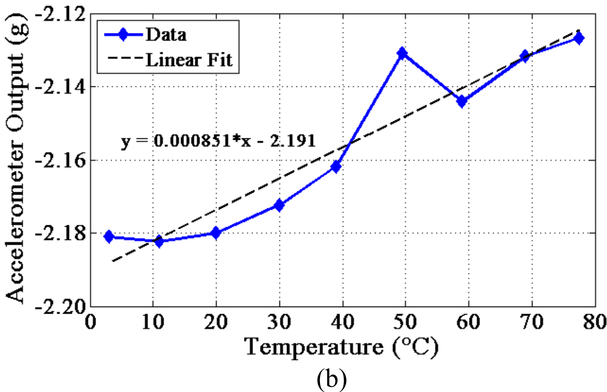

(b)

Fig. 20. The bias temperature sensitivities of (a) the lateral and (b) vertical accelerometers have been extracted as 1.6 mg/°C and 0.85 mg/°C, respectively.

performed in the range of 0 °C and 80 °C using an oven. After the measurement, the temperature sensitivities of the lateral and vertical accelerometers have been extracted as 1.6 mg/°C and 0.85 mg/°C, respectively. Figure 20 shows the bias temperature sensitivities of the lateral and vertical accelerometers.

In the literature, the reason of the deviation of the device output is associated with thermomechanical and mechanical stresses which are introduced during the assembling of the accelerometer package. Furthermore, the external loads imposed during the use in the field have effect on the bias stability [28]. Therefore, the long term stability performance of the current accelerometers may be improved by using different types of accelerometer packages and die attachment materials minimizing the stress on the sensor. The bias temperature sensitivity of the current accelerometer may be related with mismatch in the coefficient of thermal expansion (CTE) of the glass and silicon multi-stack structure.

Table VIII presents a comparison of the device performance for the three-axis accelerometer presented in the study with respect to three-axis accelerometers implemented on the same die for commercial and academic purposes. As it can be seen from this table, the three-axis accelerometer in this study provides a low noise while allowing to acceleration measurement in a reasonable range, as well as low cross-axis sensitivity and low non-linearity, compared to its counterparts.

VI. CONCLUSION

A bulk-micromachined monolithic three-axis accelerometer implemented with individual lateral and vertical accelerometers is demonstrated with low noise and high performance. The size of the fabricated three-axis accelerometer is 12 mm × 7 mm × 1 mm. The three-axis accelerometer is fabricated by using the Double Glass Modified Silicon-on-Glass (DGM-SOG) fabrication process.

This fabrication method uses the second glass wafer not only for allowing to implement a top electrode for the vertical accelerometer but also for acting as an inherent cap for the entire three-axis accelerometer structure. This cap layer does not provide hermetic sealing for individual three-axis accelerometer dies, but it still provides a protection during the dicing, as a non-standard dicing approach is developed. In addition, it provides protection during the attachment of the die to a package and during the regular use. If an application requires hermetic sealing of the individual dies, this can be achieved by using a cap glass wafer with vertical feedthrough lines, at the expense of its additional cost.

The x- and y-axis accelerometers demonstrate measured noise floors and bias instabilities equal to or better than

5.5 μg/$\sqrt{}$Hz and 2.2 μg, respectively, while the z-axis accelerometer demonstrates 12.6 μg/$\sqrt{}$Hz noise floor and 17.4 μg bias instability values using hybrid-connected fourth-order sigma-delta CMOS ASIC chips. These low noise performances are achieved with a measurement range of over $\pm$10 g for the x- and y-axis accelerometers and +12/−7.5 g for the z-axis accelerometer with non-linearity values equal to or less than 0.41%. The long term bias stability of the fabricated three-axis accelerometer is also monitored, and it is determined as 2 mg and 35 mg output drift for the lateral and vertical accelerometers, respectively. Further analysis is also performed for the bias temperature sensitivity of the fabricated three-axis accelerometer, and the bias temperature sensitivities of the lateral and vertical accelerometers have been extracted as 1.6 mg/°C and 0.85 mg/°C, respectively.

Although the demonstrated noise performance and bias instability values of the fabricated three-axis accelerometer are equal or better than 12.6 μg/$\sqrt{}$Hz noise floor and 17.4 μg bias instability values, the current three-axis accelerometer still needs some improvements on the symmetric operation of the z-axis accelerometer and the long term bias stability issues. The symmetric operation of the z-axis accelerometer can be achieved by reducing the buckling problem. This problem is inherent in multi-stack structures with different layers, even if the individual layers do not have any stress gradient, but its effect can be minimized by changing design parameters of the devices, such as the structural thickness, the spring widths, and the amount of proof mass. After determining the optimum structural thickness for the vertical accelerometer, it is easier to implement the lateral accelerometers with a matching performance to the vertical one. It is also expected that the minimization of the buckling may also positively affect the long term bias stability performance of the current accelerometer. Furthermore, the different types of accelerometer packages as well as the die attachment materials should also be researched to improve the long term stability performance of the current accelerometer. Moreover, the effect of temperature on the bias stability of the current three-axis accelerometer can be calibrated by the temperature compensation methods. This can allow to obtain a three-axis capacitive MEMS accelerometer that can potentially be used in high-end and even navigation grade applications.

Acknowledgment

The authors would like to thank to Prof. H. Kulah and U. Sonmez for their contribution to the readout electronics. The authors would also like to thank O. Akar, Dr. A. Aydemir, and Dr. S. E. Alper for their useful discussions and helps.

References

[1] D. K. Shaeffer, "MEMS inertial sensors: A tutorial overview," *IEEE Commun. Mag.*, vol. 51, no. 4, pp. 100–109, Apr. 2013.
[2] N. F. Watson, "Accelerometer system," U.S. Patent 4 601 206 A, Jul. 22, 1986.
[3] H. Luo, G. Zhang, L. R. Carley, and G. K. Fedder, "A post-CMOS micromachined lateral accelerometer," *J. Microelectromech. Syst.*, vol. 11, no. 3, pp. 188–195, Jun. 2002.
[4] B. E. Boser and R. T. Howe, "Surface micromachined accelerometers," *IEEE J. Solid-State Circuits*, vol. 31, no. 3, pp. 366–375, Mar. 1996.
[5] S. T. Cho, "Batch-dissolved wafer process for low-cost sensor applications," *Proc. SPIE*, vol. 2639, pp. 10–17, Sep. 1995.
[6] M. M. Torunbalci, E. Tatar, S. E. Alper, and T. Akin, "Comparison of two alternative silicon-on-glass microfabrication processes for MEMS inertial sensors," *Proc. Eng.*, vol. 25, pp. 900–903, Sep. 2011.
[7] B. Puers and D. Lapadatu, "Extremely miniaturized capacitive movement sensors using new suspension systems," *Sens. Actuators A, Phys.*, vol. 41, nos. 1–3, pp. 129–135, Apr. 1994.
[8] R. Puers and S. Reyntjens, "The characterization of a miniature silicon micromachined capacitive accelerometer," *J. Micromech. Microeng.*, vol. 8, no. 2, pp. 127–133, Jan. 1998.
[9] M. Pastre *et al.*, "A 300Hz 19b DR capacitive accelerometer based on a versatile front end in a 5th-order $\Delta\Sigma$ loop," in *Proc. ESSCIRC*, Athens, Greece, Sep. 2009, pp. 288–291.
[10] M. A. Lemkin, B. E. Boser, D. Auslander, and J. H. Smith, "A 3-axis force balanced accelerometer using a single proof-mass," in *Proc. Transducers*, Chicago, IL, USA, Jun. 1997, pp. 1185–1188.
[11] S.-C. Lo, C.-K. Chan, W.-C. Lai, M. Wu, Y.-C. Lin, and W. Fang, "Design and implementation of a novel poly-Si single proof-mass differential capacitive-sensing 3-axis accelerometer," in *Proc. TRANSDUCERS EUROSENSORS*, Barcelona, Spain, Jun. 2013, pp. 1819–1822.
[12] C.-M. Sun, M.-H. Tsai, Y.-C. Liu, and W. Fang, "Implementation of a monolithic single proof-mass tri-axis accelerometer using CMOS-MEMS technique," *IEEE Trans. Electron Devices*, vol. 57, no. 7, pp. 1670–1679, Jul. 2010.
[13] Y.-W. Hsu, J.-Y. Chen, H.-T. Chien, S. Chen, S.-T. Lin, and L.-P. Liao, "New capacitive low-*g* triaxial accelerometer with low cross-axis sensitivity," *J. Micromech. Microeng.*, vol. 20, no. 5, pp. 1–10, Feb. 2010.
[14] *ADXL377-Small, Low Power, 3-Axis ±200 g Accelerometer*, Analog Devices, Norwood, MA, USA, 2012.
[15] *ADXL330-Small, Low Power, 3-Axis ±3 g iMEMS Accelerometer*, Analog Devices, Norwood, MA, USA, 2007.
[16] J. Chae, H. Kulah, and K. Najafi, "A monolithic three-axis micro-g micromachined silicon capacitive accelerometer," *J. Microelectromech. Syst.*, vol. 14, no. 2, pp. 235–242, Apr. 2005.
[17] Y.-C. Liu, M.-H. Tsai, S.-S. Li, and W. Fang, "A fully-differential, multiplex-sensing interface circuit monolithically integrated with tri-axis pure oxide capacitive CMOS-MEMS accelerometers," in *Proc. TRANSDUCERS EUROSENSORS XXVII*, Barcelona, Spain, Jun. 2013, pp. 610–613.
[18] S. Tez and T. Akin, "Comparison of two alternative fabrication processes for a three-axis capacitive MEMS accelerometer," *Proc. Eng.*, vol. 47, pp. 342–345, Sep. 2012.
[19] V. Dragoi, T. Glinsner, P. Hangweier, and P. Lindner, "Triple-stack anodic bonding for MEMS applications," in *Proc. Electrochem. Soc. Meeting*, vol. PV2003-19, 2003, p. 329.
[20] E. Tatar, M. M. Torunbalci, S. E. Alper, and T. Akin, "A method and electrical model for the anodic bonding of SOI and glass wafers," in *Proc. 25th IEEE Int. Conf. Micro Electro Mech. Syst. (MEMS)*, Paris, France, Jan./Feb. 2012, pp. 68–71.
[21] U. Sönmez, H. Külah, and T. Akın, "A $\Sigma\Delta$ micro accelerometer with 6 μg/$\sqrt{}$Hz resolution and 130 dB dynamic range," *Analog Integr. Circuits Signal Process.*, vol. 81, no. 2, pp. 471–485, Nov. 2014.
[22] M.-H. Tsai, Y.-C. Liu, and W. Fang, "A three-axis CMOS-MEMS accelerometer structure with vertically integrated fully differential sensing electrodes," *J. Microelectromech. Syst.*, vol. 21, no. 6, pp. 1329–1337, Dec. 2012.
[23] H. Qu, D. Fang, and H. Xie, "A monolithic CMOS-MEMS 3-axis accelerometer with a low-noise, low-power dual-chopper amplifier," *IEEE Sensors J.*, vol. 8, no. 9, pp. 1511–1518, Sep. 2008.
[24] *BMA355 Digital, Triaxial Acceleration Sensor*, Bosch, Reutlingen, Germany, document BST-BMA355-FL000-00/Version_0.5_0.3, 2013.
[25] *H3LIS331DL-MEMS Motion Sensor: Low-Power High-G 3-Axis Digital Accelerometer*, STMicroelectronics, document DocID23111 Rev.3, 2013.
[26] *Xtrinsic MMA8452Q 3-Axis, 12-Bit/8-Bit Digital Accelerometer*, Freescale Semiconductor, document MMA8452Q, 2014.
[27] *AIS328DQ-High-Performance Ultra Low-Power 3-Axis accelerometer With Digital Output for Automotive Applications*, STMicroelectronics, document 18160, 2012.
[28] X. Zhang, S. Park, and M. W. Judy, "Accurate assessment of packaging stress effects on MEMS sensors by measurement and sensor–package interaction simulations," *J. Microelectromech. Syst.*, vol. 16, no. 3, pp. 639–649, Jun. 2007.

Serdar Tez received the B.S and M.S. degrees from the Physics Department, Suleyman Demirel University, Isparta, Turkey, in 2004 and 2006, respectively, and the Ph.D. degree from the Micro and Nanotechnology Graduate Program, Middle East Technical University (METU), Ankara, Turkey, in 2014, with a focus on microelectromechanical systems (MEMS) three-axis capacitive accelerometers. He joined the METU-MEMS Research and Applications Center in 2008. He is currently with the Department of Electrical and Electronics Engineering, Pamukkale University, Denizli, Turkey. His current research interests are the design, simulation, and fabrication methods of microstructures.

Ulas Aykutlu was born in Izmir, Turkey, in 1989. He received the B.S. degree in electrical and electronics engineering from Middle East Technical University (METU), Ankara, Turkey, in 2012, where he is currently pursuing the M.Sc. degree in electrical and electronics engineering. He has been a Research Assistant with the Micro-Electro-Mechanical Systems Research and Applications Center, METU, since 2012. His research interests include capacitive interface circuits, sigma–delta modulators, and switched capacitor circuits.

Mustafa Mert Torunbalci was born in Ankara, Turkey, in 1985. He received the B.S. degree from the Department of Physics Engineering, Ankara University, Ankara, in 2008, and the M.Sc. and Ph.D. degrees from the Department of Micro and Nanotechnology, Middle East Technical University (METU), Ankara, in 2011 and 2015, respectively.

He has been a Research Assistant with the METU-MEMS Research and Applications Center since 2008. His major research interests include the design, simulation, fabrication, and wafer level packaging of microelectromechanical systems inertial sensors.

Tayfun Akin was born in Van, Turkey, in 1966. He received the B.S. (Hons.) degree in electrical engineering from Middle East Technical University (METU), Ankara, in 1987, and the M.S. and Ph.D. degrees in electrical engineering from the University of Michigan, Ann Arbor, in 1989 and 1994, respectively. He went to the USA in 1987 for his graduate studies with a graduate fellowship provided by the NATO Science Scholarship Program through the Scientific and Technical Research Council of Turkey. Since 1995, 1998, and 2004, he has been an Assistant Professor, an Associate Professor, and a Professor, respectively, with the Department of Electrical and Electronics Engineering, METU. He is the Director of the METU-Microelectromechanical Systems (MEMS) Center. He raised and managed over 65M USD funding for several national and international projects, including EU FP6, FP7, NATOSfS, and NSF-USA Projects. His current research interests include MEMS, microsystems technologies, uncooled infrared detectors and readout circuits, inertial microsensors, silicon-based integrated sensors and transducers, and analog and digital integrated circuit design. He has served in various MEMS, EUROSENSORS, and TRANSDUCERS Conferences as a Technical Program Committee Member. He was the Co-Chair of the 19th IEEE International Conference of Micro Electro Mechanical Systems (MEMS 2006) in Istanbul, and the Co-Chair of the Steering Committee of the IEEE MEMS Conference in 2007. He is the Steering Committee Member of the 18th International Conference on Solid-State Sensors, Actuators, and Microsystems (Transducers 2015). He is a recipient of the First Prize in Experienced Analog/Digital Mixed-Signal Design Category at the 1994 Student VLSI Circuit Design Contest, organized and sponsored by Mentor Graphics, Texas Instruments, Hewlett-Packard, Sun Microsystems, and *Electronic Design Magazine*. He has co-authored the Symmetric and Decoupled Gyroscope project, which received the First Prize Award in the operational designs category of the international design contest, organized by the DATE Conference and CMP in 2001. He has co-authored the Gyroscope project, which received the Third Prize Award of the 3-D MEMS Design Challenge, organized by MEMGen Corporation (currently, Microfabrica).